25. M. Rini, D. Pines, B.-Z. Magnes, E. Pines, E. T. J. Nibbering, *J. Chem. Phys.* **121**, 9593 (2004).
26. Details of the experimental methods and modeling can be found on *Science* Online.
27. Because the photobase band at 1503 cm^{-1} strongly overlaps with two transitions of HPTS in the photo-acid state, its magnitude at early pulse delays cannot be determined accurately.
28. E. Pines, D. Huppert, N. Agmon, *J. Chem. Phys.* **88**, 5620 (1988).
29. O. F. Mohammed, J. Dreyer, B.-Z. Magnes, E. Pines, E. T. J. Nibbering, *ChemPhysChem* **6**, 625 (2005).
30. B. S. Ault, G. C. Pimentel, *J. Phys. Chem.* **77**, 57 (1973).
31. J. M. Williams, in *The Hydrogen Bond: Recent Developments in Theory and Experiments*, vol. 2,

Structure and Spectroscopy, P. Schuster, G. Zundel, C. Sandorfy, Eds. (North Holland, Amsterdam, 1976), pp. 655.
32. L. Delzeit, B. Rowland, J. P. Devlin, *J. Phys. Chem.* **97**, 10312 (1993).
33. M. Okumura, L. I. Yeh, J. D. Myers, Y. T. Lee, *J. Phys. Chem.* **94**, 3416 (1990).
34. R. Rousseau, V. Kleinschmidt, U. W. Schmitt, D. Marx, *Angew. Chem. Int. Ed.* **43**, 4804 (2004).
35. S. A. Corcelli, J. L. Skinner, *J. Phys. Chem. A* **109**, 6154 (2005).
36. N. Agmon, *Chem. Phys. Lett.* **244**, 456 (1995).
37. We also performed experiments with dichloro- and trichloroacetate as bases. The results show similar behavior to that of monochloroacetate but with even longer lifetimes of the intermediate ionic complexes.

38. S. Meiboom, *J. Chem. Phys.* **34**, 375 (1961).
39. This research has been supported by the German-Israeli Foundation for Scientific Research and Development (project GIF 722/01) and a long-term mission fellowship of the Egyptian government for O.F.M.

PbSe Nanocrystal Solids for n- and p-Channel Thin Film Field-Effect Transistors

Dmitri V. Talapin* and Christopher B. Murray

Initially poorly conducting PbSe nanocrystal solids (quantum dot arrays or superlattices) can be chemically "activated" to fabricate n- and p-channel field effect transistors with electron and hole mobilities of 0.9 and 0.2 square centimeters per volt-second, respectively; with current modulations of about 10^3 to 10^4; and with current density approaching 3×10^4 amperes per square centimeter. Chemical treatments engineer the interparticle spacing, electronic coupling, and doping while passivating electronic traps. These nanocrystal field-effect transistors allow reversible switching between n- and p-transport, providing options for complementary metal oxide semiconductor circuits and enabling a range of low-cost, large-area electronic, optoelectronic, thermo-electric, and sensing applications.

Solution-based processes such as spin coating, dip coating, and inkjet printing offer substantial cost reductions for the fabrication of electronic and optoelectronic devices when combined with materials such as organic semiconductors (*1*), carbon nanotubes (*2*), nanowires (*3*), soluble precursors for inorganic semiconductors (*4*), and hybrid organic-inorganic films (*5*). However, none of these approaches can yet enable devices with performance comparable to that of conventional inorganic crystalline semiconductors. Improvement of the electronic performance in these systems comes at the price of high-precision and low-throughput fabrication techniques (*3*) or else requires high-temperature anneals that limit compatibility with flexible plastic substrates. The trade-off between device performance and fabrication costs motivates the search for new classes of materials for low-cost electronics. Here, we report the assembly of solid-state field-effect transistors (FETs) from solution-processable semiconductor nanocrystals.

Charge transport in an array of nanocrystals separated by insulating capping ligands (a "nanocrystal solid") depends on matching of the energy levels of neighboring nanocrystals (site energies, α), on the exchange coupling energy between the nanocrystals (β), and on the Coulomb charging energy of the nanocrystal array (E_c) (*6, 7*). For efficient charge transport, the dispersion of site energies $\Delta\alpha$ should not exceed β, or Anderson localization will dominate. If $\beta < E_c$, the nanocrystal array can behave as a Mott insulator (*8*).

Past studies have revealed low electronic conductivity in semiconductor nanocrystal arrays because of poor exchange coupling and large concentrations of surface dangling bonds that trap carriers in mid-gap states (*9–12*). Sintering individual nanocrystals into a polycrystalline film increases film conductance but leaves structural defects that limit the device switching speeds (*13*). Another approach to enhance electron mobility in a nanocrystal solid is based on cross-linking of the nanocrystals by conjugated organic molecules (e.g., 1,4-phenylenediamine) followed by electrochemical charging with several additional electrons per nanocrystal (*14–16*). Charge screening by the electrolyte's mobile ions substantially reduces E_c, facilitating the nanocrystal charging (*12*). The mobility increases because of a combination of trap filling and the participation of multiple quantum confined electronic states (1S, 1P, etc.) in charge transport (*12, 14*). However, technological implementations require FETs with insulated gates capacitively coupled to the transistor channel.

We selected PbSe nanocrystals because they allow smaller $\Delta\alpha$ and E_c and larger β values, compared to the extensively studied CdSe and ZnO nanocrystal solids. In an ensemble of strongly confined semiconductor nanocrystals, charge transport occurs between electronic quantum confined orbitals (*12*), and $\Delta\alpha$ can be estimated from the linewidth of the first excitonic ($1S_h$-$1S_e$) transition (*15*). We optimized the synthesis (*16*) to obtain monodisperse (<5% SD) PbSe nanocrystals, with the full width at half maximum of the $1S_h$-$1S_e$ transition below 40 meV (Fig. 1, A and B). The 1S quantum confined orbitals in rock-salt PbSe nanocrystals are eight-fold degenerated (*17*) versus the two-fold spin degeneracy in II-VI nanocrystals. Higher degeneracy and narrower linewidth provide a higher density of electronic states (DOS) available for the charge transport. In a close-packed array of 8-nm PbSe nanocrystals, the densities of $1S_h$ and $1S_e$ states are each $\sim 5 \times 10^{20}$ eV^{-1} cm^{-3}, an order of magnitude higher than the DOS in arrays of CdSe or ZnO nanocrystals of the same size and ~ 330 times the DOS in amorphous germanium (*15*).

The exchange coupling energy scales approximately as $\beta \sim \exp[-\kappa(d + \delta)]$, where d is the nanocrystal diameter, δ is the interparticle spacing, and κ^{-1} describes the length scale of the wave function leakage outside the nanocrystal (*6, 7*). The large Bohr radius of electrons and holes in PbSe (~ 23 nm in both) suggests that their wave functions spill far outside the volume of the nanocrystal, facilitating exchange interactions.

The charging energy E_c of a spherical nanocrystal can be estimated as $E_c = e^2/(4\pi\varepsilon_m\varepsilon_0 d)$ where ε_m is the dielectric constant of the surrounding medium. The dialectric constant for bulk PbSe is very high ($\varepsilon \sim 250$, as compared to $\varepsilon \sim 6.2$ for CdSe), with $\varepsilon > 100$ measured for individual 12-nm PbSe nanocrystals (*18*). This predicts an E_c of <4 meV for a three-

IBM Research Division, T. J. Watson Research Center, 1101 Kitchawan Road, Yorktown Heights, NY 10598, USA.

*To whom correspondence should be addressed. E-mail: dmitrit@us.ibm.com

dimensional array of 8-nm PbSe nanocrystals, which is a small fraction of thermal energy at room temperature (k_BT, where k_B is the Boltzmann constant and T is the temperature) and an order of magnitude smaller than E_c for analogous CdSe nanocrystal arrays (*16*).

For electronic studies, close-packed PbSe nanocrystal films, 35 ± 10 nm thick, were deposited on highly doped Si wafers with 100-nm-thick SiO_2 thermal gate oxide. Source and drain Ti/Au (75/375 Å) electrodes spaced from 4 μm to 40 μm apart were patterned on the SiO_2 surface before nanocrystal deposition (*16*).

Small angle x-ray scattering at grazing incidence (GISAXS) from 8-nm PbSe nanocrystals assembled in the channel between parallel electrodes showed well-resolved reflections (Fig. 1C), confirming both in-plane and vertical particle ordering in a film that was drop-cast from a hexane:octane (9:1 by volume) solution. The parallel source and drain electrodes directed the crystallographic orientation of growing superlattices (fig. S1). Moreover, close-packed PbSe nanocrystals showed strong preferential orientation of their atomic lattices, favorable for charge transport through P-quantized states (figs. S2 and S3).

As-deposited PbSe nanocrystal arrays were insulating, with a conductance (G) less than 10^{-11} S cm^{-1}, because of ~1.5-nm interparticle spacing maintained by insulating oleic acid molecules (Fig. 1B). Thorough washing of the nanocrystal colloids (*16*) removed a fraction of the native capping groups, reducing interparticle spacing to ~1.1 nm and yielding a higher conductance of $G \sim 3 \times 10^{-10}$ S cm^{-1}. However, the removal of capping groups introduced pronounced hysteresis in the current-voltage (*I-V*) scans (Fig. 2A), probably due to filling of traps associated with surface dangling bonds. No gate modulation was observed in the native nanocrystal films.

The conductance of PbSe nanocrystal solids increased by ~10 orders of magnitude after treatment with a 1.0 M solution of hydrazine in acetonitrile (Fig. 2B) (*16*). The current through the nanocrystal film can be modulated by application of a potential to the back gate electrode, producing an n-FET (*1*) (Fig. 2C). Figure 3A shows a current modulation I_{on}/I_{off} of ~2.5 × 10^3 for a PbSe nanocrystal n-FET, with minor hysteresis between gate voltage (V_G) scans in the forward and reverse directions (fig. S4). In the "on" state, low-field conductance of PbSe nanocrystal film was ~0.82 S cm^{-2} (V_G = 40 V), and the current density in the saturation regime approached 2.7 × 10^4 A cm^{-2}. Extracting field-effect electron mobilities (μ) from a series of devices yielded $\mu_{lin} \sim 0.4$ cm^2 V^{-1} s^{-1} in the linear regime and $\mu_{sat} \sim 0.7$ cm^2 V^{-1} s^{-1} in the saturation regime (*16*). The μ_{sat} values increased with nanocrystal size. The highest mobility, $\mu_{sat} = 0.95$ cm^2 V^{-1} s^{-1}, was observed for 9.2-nm PbSe nanocrystals.

Vacuum treatment or mild heating (to ~100°C) of activated PbSe nanocrystal films switched their conductivity from n-type (Fig. 3A) to ambipolar (Fig. 3B) and, finally, to p-type (Fig. 3, C and D) as the hydrazine desorbed. The resulting p-FETs showed room-temperature hole mobilities μ_{sat} of 0.12 to 0.18 cm^2 V^{-1} s^{-1}, current modulations of ~10^2 (Fig. 3D), and "on" state current densities approaching ~3 × 10^3 A cm^{-2}. At 120 K, current modulation increased to ~1.6 × 10^4, whereas the hole mobility decreased to $\mu_{sat} = 0.09$ cm^2 V^{-1} s^{-1} and was almost independent of the gate voltage (Fig. 3C). The hole transport in PbSe nanocrystal solids most probably occurs through the 1S$_h$ orbitals (*19*). Switching between electron and hole transport was reversible upon re-exposure to hydrazine, allowing fabrication of complementary metal oxide semiconductor circuits.

Scanning and transmission electron microscopy (SEM and TEM) and x-ray diffraction studies showed that the hydrazine treatment did not change nanocrystal size or shape but markedly reduced the interparticle spacing (Fig. 4A and fig. S3). The reflections in GISAXS patterns shifted to higher scattering (2θ) angles, showing that interparticle spacing decreased by 0.8 nm, i.e., from ~1.1 nm to ~0.3 nm (Fig. 4B) (*16*). Once hydrazine-treated, films neither dissolved nor swelled on re-exposure to nonpolar solvents. This allowed us to pattern PbSe nanocrystal films. Local exposure to hydrazine solutions rendered the regions conductive, whereas unexposed film could be lifted off in hexane. Sequential layer-by-layer deposition would allow different material combinations, e.g., p- and n-conducting layers for designing nanocrystal-based photovoltaic cells.

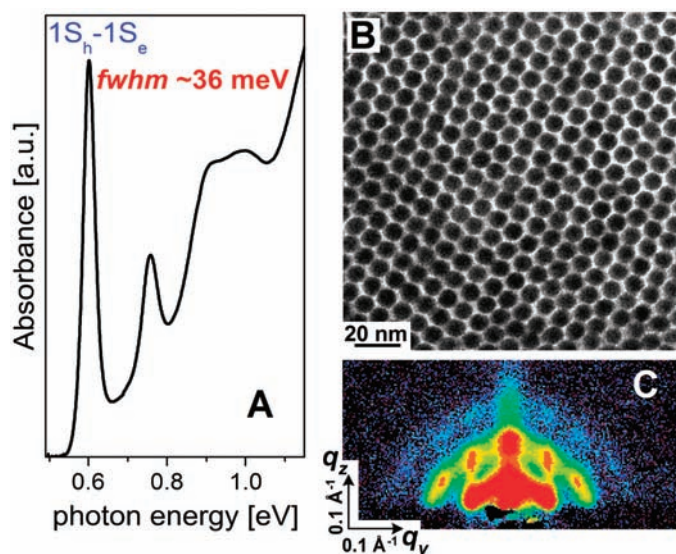The absorption spectra of the conductive PbSe nanocrystal films show excitonic peaks

Fig. 1. (A) Optical absorption spectrum of a colloidal solution of 8-nm PbSe nanocrystals in tetrachloroethylene. a.u., arbitrary units; fwhm, full width at half-maximum. (B) TEM image of an array of 8-nm PbSe nanocrystals. q_y and q_z are the lateral and vertical components of the momentum transfer, respectively. (C) GISAXS pattern of PbSe nanocrystal film (*16*).
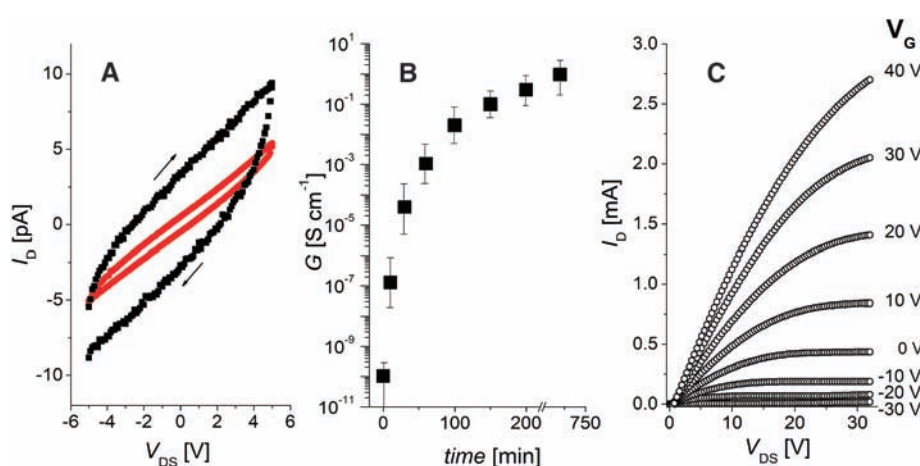

Fig. 2. (A) *I-V* scans for a film of 8-nm oleic acid capped PbSe nanocrystals in which the voltage scan rate is 0.5 V s^{-1} (black) and 0.025 V s^{-1} (red) and the channel length L and width W are 6 μm and 5000 μm, respectively. (B) Conductance G of a PbSe nanocrystal film versus time of exposure to a 1 M solution of N_2H_4 in acetonitrile. The error bars show the spread in data from five samples. (C) Plot of drain current I_D versus drain-source voltage V_{DS}, as a function of V_G for a nanocrystal FET with a channel composed of 8-nm PbSe nanocrystals treated with hydrazine solution for 12 hours (L = 10 μm, W = 2000 μm, with a 100-nm-thick SiO_2 gate dielectric).

that shifted by ∼20 meV to lower energy relative to native insulating films (Fig. 4C). The persistence of excitonic peaks implies the electron and hole wave functions either remain localized on the individual PbSe nanocrystals or form narrow minibands due to exchange coupling (20). At low temperatures, charge transport in PbSe nanocrystal solids occurred through variable range hopping, as confirmed by linearization of low-field conductance in the Mott coordinates ($\ln G \sim T^{-1/4}$) (8) (fig. S5).

The hydrazine treatment can simultaneously tune β, E_c, trap density, and the doping level

of a PbSe nanocrystal solid. Hydrazine is a Brönsted base and can gently react to remove and replace the bulky oleic acid capping ligands from the nanocrystal surface, reducing the interparticle spacing and increasing β. Hydrazine is also a strong Lewis base with lone pairs of electrons that can saturate dangling bonds at the nanocrystal surface in analogy to primary amines (21). We might also speculate about linking PbSe nanocrystals by bidentate hydrazine molecules, as the mean interparticle spacing is close to the length of a hydrazine molecule. Hydrazine is a reducing agent, pre-

venting oxidation of PbSe nanocrystals and "repairing" any oxidized selenium surface sites that might generate mid-gap levels (22). Replacement of oleic acid (ε ∼ 2) with hydrazine (ε ∼ 52) also substantially reduces E_c. The increase of β and decrease of E_c helps to close the Hubbard gap (8), enabling the insulator-metal Mott transition in the nanocrystal solid. Finally, hydrazine behaves as a charge-transfer n-type dopant, as has been observed for PbSe nanowires (23) and carbon nanotubes (24).

Annealing the activated PbSe nanocrystal films at ∼200°C for 1 hour and re-exposing them to a hydrazine solution allowed us to achieve degenerate doping and metallic conductivity ($G \sim 8.5$ S cm^{-2}) (fig. S6). The semiconductor-metal transition was reversible, as partial stripping of the hydrazine (6 hours at 40°C under nitrogen) yielded n-type semiconducting films with high electron mobility ($\mu_{lin} \sim 2.5$ cm^2 V^{-1} s^{-1}) (fig. S7), thus demonstrating that tailoring of β and the doping density allows controllable switching between insulating, semiconducting, and metallic states in PbSe nanocrystal solids.

Colloidal nanocrystals can now enable room-temperature fabrication of n- and p-channel field effect devices by inexpensive and high-throughput solution-based processes. We observed good performance for PbSe nanocrystal FETs, even for long (e.g., 40 μm) channels (fig. S8). Such device dimensions are easily accessible by stamping or inkjet-printing. The observed field-effect mobilities in PbSe nanocrystal films are comparable to the hole mobility in pentacene films (2), although lower than the electron mobility in the best solution-processed inorganic semiconductors (4).

The hydrazine treatment is a general technique for increasing conductance in nanocrystal solids. In addition to PbSe FETs, we have assembled operational solid-state FETs from PbS, PbTe, CdSe, and InP nanocrystals and CdSe nanorods, thus demonstrating the applicability of our approach to different materials.
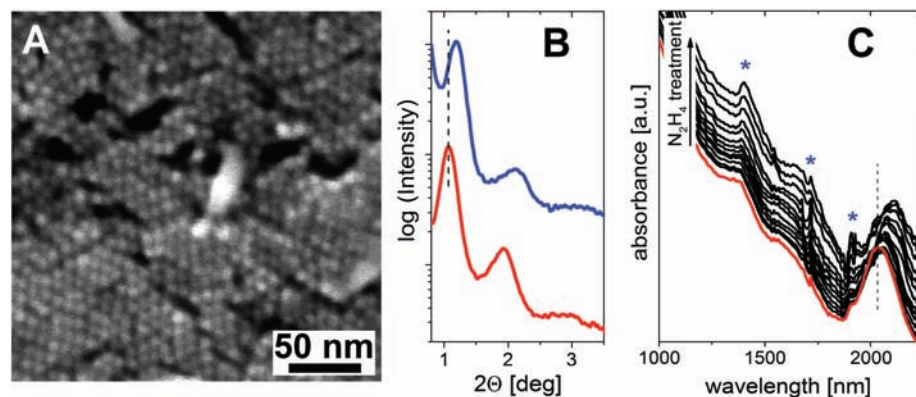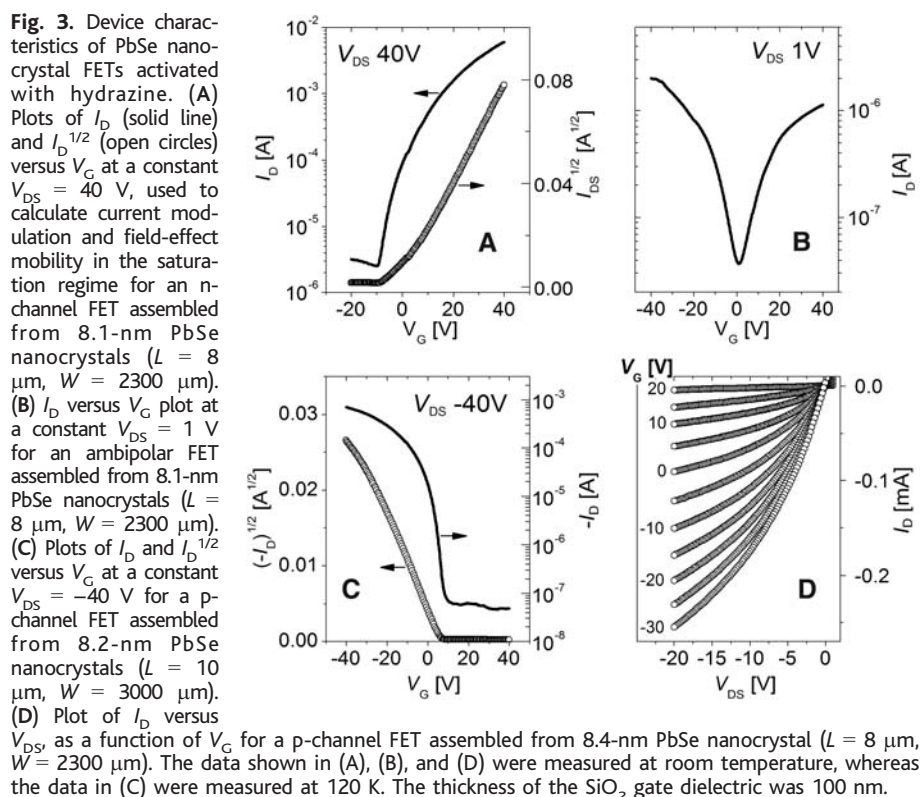

Fig. 3. Device characteristics of PbSe nanocrystal FETs activated with hydrazine. (A) Plots of I_D (solid line) and $I_D^{1/2}$ (open circles) versus V_G at a constant V_{DS} = 40 V, used to calculate current modulation and field-effect mobility in the saturation regime for an n-channel FET assembled from 8.1-nm PbSe nanocrystals (L = 8 μm, W = 2300 μm). (B) I_D versus V_G plot at a constant V_{DS} = 1 V for an ambipolar FET assembled from 8.1-nm PbSe nanocrystals (L = 8 μm, W = 2300 μm). (C) Plots of I_D and $I_D^{1/2}$ versus V_G at a constant V_{DS} = −40 V for a p-channel FET assembled from 8.2-nm PbSe nanocrystals (L = 10 μm, W = 3000 μm). (D) Plot of I_D versus V_{DS}, as a function of V_G for a p-channel FET assembled from 8.4-nm PbSe nanocrystal (L = 8 μm, W = 2300 μm). The data shown in (A), (B), and (D) were measured at room temperature, whereas the data in (C) were measured at 120 K. The thickness of the SiO$_2$ gate dielectric was 100 nm.

Fig. 4. (A) High-resolution SEM image of a PbSe nanocrystal film treated with a 1 M N$_2$H$_4$ solution for 12 hours. (B) Small-angle x-ray scattering from an array of 8.1-nm PbSe nanocrystals before (red) and after (blue) the hydrazine treatment. 2θ, scattering angle. (C) Evolution of the absorption spectrum of the 7.5-nm PbSe nanocrystal film with time during a 4-hour hydrazine treatment (16). The initial absorption spectrum is shown in red. The infrared absorption bands from the solvent are marked by blue asterisks, and the dashed line indicates the position of the 1S$_h$-1S$_e$ excitonic transition in the initial, insulating nanocrystal film.

References and Notes
1. C. R. Kagan, P. Andry, Eds., *Thin Film Transistors* (Marcel Dekker, New York, 2003).
2. E. Artukovic, M. Kaempgen, D. S. Hecht, S. Roth, G. Gruner, *Nano Lett.* **5**, 841 (2005).
3. X. Duan et al., *Nature* **425**, 274 (2003).
4. D. B. Mitzi, L. L. Kosbar, C. E. Murray, M. Copel, A. Afzali, *Nature* **428**, 299 (2004).
5. C. R. Kagan, D. B. Mitzi, C. D. Dimitrakopoulos, *Science* **286**, 945 (1999).
6. F. Remacle, K. C. Beverly, J. R. Heath, R. D. Levine, *J. Phys. Chem. B* **107**, 13892 (2003).
7. C. P. Collier, R. J. Saykally, J. J. Shiang, S. E. Henrichs, J. R. Heath, *Science* **277**, 1978 (1997).
8. N. F. Mott, *Conduction in Non-Crystalline Materials* (Clarendon, Oxford, 1993), ed 2.
9. N. Y. Morgan et al., *Phys. Rev. B* **66**, 075339 (2002).
10. M. B. Jarosz, V. J. Porter, B. R. Fisher, M. A. Kastner, M. G. Bawendi, *Phys. Rev. B* **70**, 195327 (2004).
11. D. S. Ginger, N. C. Greenham, *J. Appl. Phys.* **87**, 1361 (2000).
12. D. Vanmaekelbergh, P. Liljeroth, *Chem. Soc. Rev.* **34**, 299 (2005).
13. B. R. Ridley, B. Nivi, J. M. Jacobson, *Science* **286**, 746 (1999).

14. D. Yu, C. Wang, P. Guyot-Sionnest, *Science* **300**, 1277 (2003).
15. D. Yu, C. Wang, B. L. Wehrenberg, P. Guyot-Sionnest, *Phys. Rev. Lett.* **92**, 216802 (2004).
16. Materials and methods are available as supporting material on *Science* Online.
17. G. Allan, C. Dellerue, *Phys. Rev. B* **70**, 245321 (2004).
18. C. H. Ben-Porat, O. Chernyavskaya, L. Brus, K.-S. Cho, C. B. Murray, *J. Phys. Chem. B* **108**, 7814 (2004).
19. The possibility of hole injection into the $1S_h$ state of a semiconductor nanocrystal has been demonstrated by Wehrenberg and Guyot-Sionnest (*25*).
20. O. L. Lazarenkova, A. A. Balandin, *J. Appl. Phys.* **89**, 5509 (2001).
21. D. V. Talapin, A. L. Rogach, A. Kornowski, M. Haase, H. Weller, *Nano Lett.* **1**, 207 (2001).
22. J. S. Steckel, S. Coe-Sullivan, V. Bulović, M. B. Bawendi, *Adv. Mater.* **15**, 1862 (2003).
23. D. V. Talapin, unpublished data.
24. C. Klinke, J. Chen, A. Afzali, Ph. Avouris, *Nano Lett.* **5**, 555 (2005).
25. B. L. Wehrenberg, P. Guyot-Sionnest, *J. Am. Chem. Soc.* **125**, 7806 (2003).
26. We thank C. T. Black, C. R. Kagan, J. J. Urban, E. V. Shevchenko, V. Perebeinos, R. L. Sandstrom, and A. Afzali for helpful comments, suggestions, and stimulating discussions.

Nanoscale Imaging of Buried Structures via Scanning Near-Field Ultrasound Holography

Gajendra S. Shekhawat[1,2] and Vinayak P. Dravid[1,2,3]*

A nondestructive imaging method, scanning near-field ultrasound holography (SNFUH), has been developed that provides depth information as well as spatial resolution at the 10- to 100-nanometer scale. In SNFUH, the phase and amplitude of the scattered specimen ultrasound wave, reflected in perturbation to the surface acoustic standing wave, are mapped with a scanning probe microscopy platform to provide nanoscale-resolution images of the internal substructure of diverse materials. We have used SNFUH to image buried nanostructures, to perform subsurface metrology in microelectronic structures, and to image malaria parasites in red blood cells.

Nondestructive real-space imaging of deeply buried or embedded structures and features with lateral resolution below ~100 nm is a formidable challenge (*1–5*). Conventional imaging with noninvasive radiation, such as light and acoustic waves, cannot achieve useful resolution below 100 nm because of the classical diffraction limit (*6–8*). Scanning probe microscopy (SPM) and its analogs offer superb spatial resolution but are sensitive only to surface or shallow subsurface features (*9, 10*). Near-field scanning optical microscopy offers subwavelength resolution but is unable to image optically opaque and deeply buried structures (*11, 12*). Thus, with respect to nondestructive real-space imaging, there is a clear void between the two ranges of length scales offered by confocal/photon or acoustic/sonography techniques (micrometer scale) (*13–16*) and SPM (nano- and subnanometer scale) (*9, 10*), particularly if the features of interest are buried deeper into the material, beyond the interaction range of proximal probes.

The need for nondestructive nanoscale imaging of buried and embedded structures is critical for numerous materials, structures, and phenomena as the scale of fabrication continues to shrink and the micro/nanofabrication paradigm moves from planar to three-dimensional (3D) or stacked platforms. In microelectronics, for example, such metrology challenges are well articulated in the International Technology Roadmap for Semiconductors (*17*). The need for a higher resolution, nondestructive, real-space imaging approach is equally critical in biological systems for noninvasive monitoring of signal pathways, cellular transfection, and other subcellular phenomena.

In conventional nondestructive imaging approaches based on acoustic and light microscopy, classical diffraction limits the spatial resolution in the far-field regime. For example, the spatial resolution, δ, in an acoustic microscope is given by

$$\delta = 0.51(v_o/fNA) \qquad (1)$$

(*7, 8*), where v_o is the speed of sound in the coupling medium, f is the frequency of the acoustic/ultrasonic wave, and NA is the numerical aperture of the lens. Conventional far-field approaches are also limited by the need for liquid lenses and coupling fluid, among other considerations.

Several SPM-based techniques have been introduced in recent years with mixed results in the context of sensitivity to surface nanomechanical variations, ability to probe deeply buried or embedded features, or quantitative extraction of nanomechanical contrast. Force modulation microscopy (also called ultrasonic force microscopy) (*18–23*) and heterodyne force microscopy (*24*) are notable SPM-based techniques that have enjoyed some success in nanomechanical mapping of elastic and visco-

elastic properties of soft and hard surfaces. However, a wider deployment of these techniques is generally marred by lack of reproducibility, unpredictable environmental effects in the usual contact mode of imaging, and lack of compelling evidence for demonstrated sensitivity to buried and embedded structure. Moreover, these techniques use nonlinear tip-sample interactions, where the origin of the dominant mechanical contrast in the images is mainly from differential surface mechanical properties with a large physical contact between the cantilever and sample; such methods are therefore not well suited for imaging of soft materials such as polymers and biological structures.

Here we introduce an imaging approach, scanning near-field ultrasound holography (SNFUH), that is sensitive to deeply buried features, offers nanoscale lateral resolution with depth sensitivity, and is equally amenable to hard (engineered systems), soft (polymers and biological structures), and hybrid materials. In SNFUH, a high-frequency acoustic wave (on the order of megahertz or higher, substantially greater than the resonance frequency of the typical cantilever, $f_0 \sim$ 10 to 100 kHz) is launched from the bottom of the specimen while another wave is launched on the SPM cantilever, albeit at a slightly different frequency (Fig. 1). The interference of these two waves would nominally form a surface acoustic standing wave, which is analogous to, for example, x-ray standing waves that result from interference of scattered and reference x-ray waves (*25, 26*). The perturbations to the phase and amplitude of the surface acoustic standing wave are locally monitored by the SPM acoustic antenna via the lock-in approach and a SNFUH electronic module. As the specimen acoustic wave is perturbed by buried features, the resultant alteration in the surface acoustic standing wave, especially its phase, is effectively monitored by the SPM cantilever. Thus, within the near-field regime (which enjoys superb spatial resolution), the acoustic wave (which is nondestructive and sensitive to mechanical and/or elastic variation along its path) is fully analyzed, point-by-point, by the SPM acoustic antenna in terms of its phase and amplitude. Thus, as the specimen is scanned, a pictorial representation of its acoustic wave perturbation is recorded and displayed that offers a quantitative account of the internal features of the specimen.

[1]Institute for Nanotechnology, [2]NUANCE Center, [3]Department of Materials Science and Engineering, Northwestern University, Evanston, IL 60208, USA.

*To whom correspondence should be addressed. E-mail: v-dravid@northwestern.edu

Editor's Summary

This copy is for your personal, non-commercial use only.